Electronic Supplementary Material (ESI) for Chemical Science.
This journal is © The Royal Society of Chemistry 2020

ELECTRONIC SUPPLEMENTARY INFORMATION (ESI)

Light-harvesting complexes access analogue emissive states in different environments

Vincenzo Mascoli[1], Andrius Gelzinis[2,3], Jevgenij Chmeliov[2,3], Leonas Valkunas[2,3], Roberta Croce[1,*]

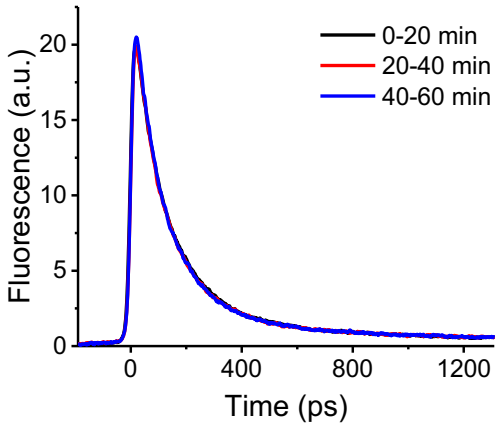

Figure S1. Fluorescence time traces acquired at 680 nm for CP29 oligomers at RT during different time intervals within the measuring time of 1 hour. The overlapping traces prove that the sample is stable during the entire measurement.

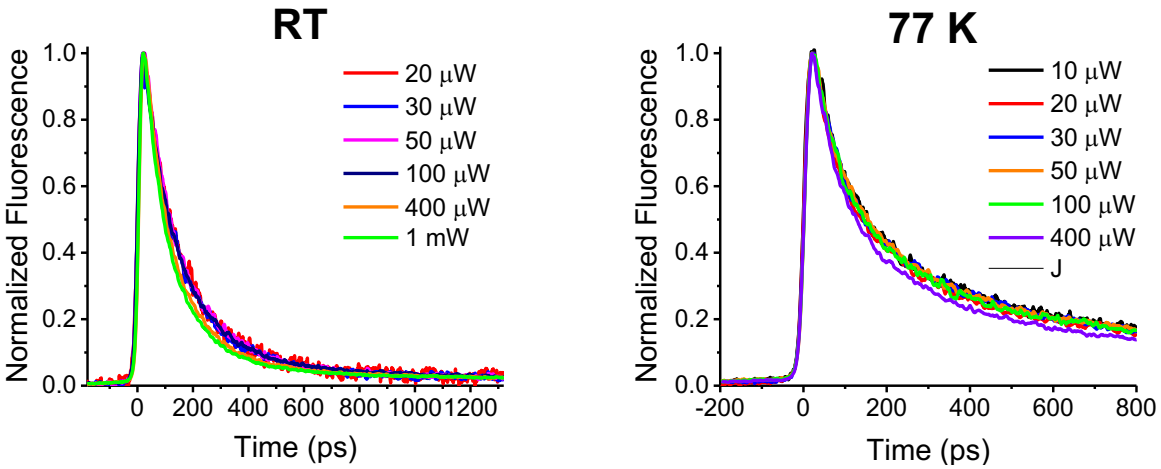

Figure S2. Fluorescence time traces acquired at 680 nm for CP29 oligomers at RT (left) and integrated in the spectral region between 680 and 720 nm for CP29 oligomers at 77 K (right) at different excitation powers. The traces are power-independent below 100 μW at both temperatures.

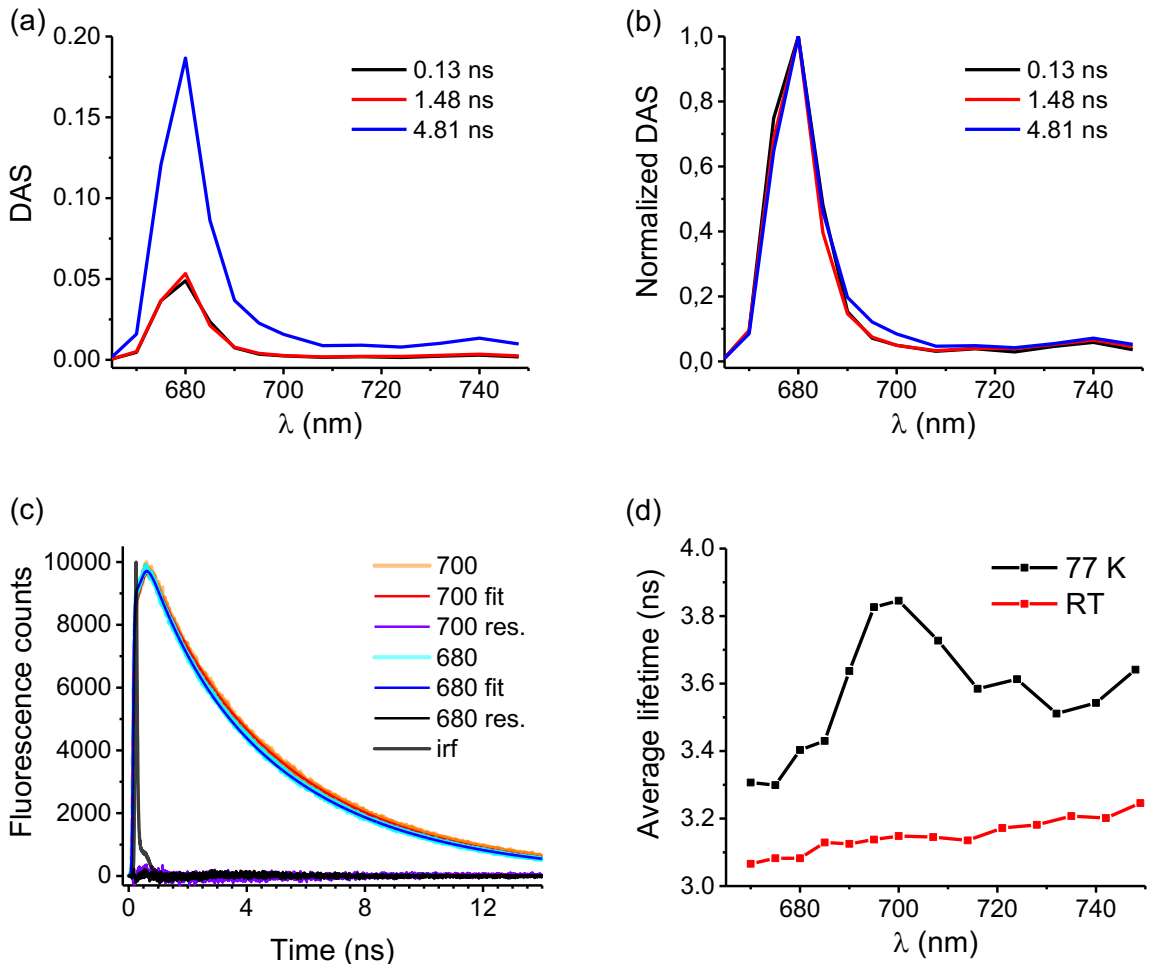

Figure S3. Time-resolved fluorescence experiments of CP29 WT monomers at 77 K**.** Top layer: decay-associated spectra (DAS, (a)) and normalized DAS ((b)) from global analysis of time-resolved fluorescence data of CP29 WT at 77 K upon 468 nm excitation. We have recently shown that, at room temperature, detergent-solubilized monomeric CP29 exhibits a heterogeneous distribution of emissive states with the same spectra but lifetimes ranging from 4 ns to less than 100 ps[1]. A similar heterogeneity is also observed at 77 K, where three main lifetime components can be resolved: as at RT, the largest fraction of CP29 is unquenched (4.8 ns, carrying 64% of the total amplitude at 680 nm, blue DAS), whereas smaller populations are found in moderately quenched (1.5 ns, 18%, red DAS) and strongly quenched (0.1 ns, 18%, black DAS) states. The lifetimes and amplitudes observed at 77 K can be easily mapped to those measured at RT, suggesting that the same emissive states are present at both temperatures with slightly different lifetimes and populations. Similar to what previously reported at RT, the normalized spectra of all three components are nearly identical at 77 K, all peaking at 680 nm. Interestingly, the longest component displays some extra-amplitude around 700 nm. In addition, the average lifetime of CP29 at 77 K has a distinct wavelength dependency, with a maximum near 700 nm. This suggests that a small amount of long-lived red-emitting complexes (with a fluorescence maximum near 700 nm) is present besides the prevailing blue-emitting states (both quenched and unquenched). This finding agrees with previous observations from LHCa's (which are constitutively redshifted) and aggregated LHCII, where the red-emitting states were shown to

be not related to quenching. (c) Measured (in transparent cyan/orange) and globally fitted (in blue/red) fluorescence time traces at 680 nm and 700 nm for CP29 WT at 77 K upon 468 nm excitation. Experimental traces are scaled to the same maximum. The difference between measured and fitted data (residuals) is displayed in black/violet, while the instrument response function (IRF), measured with pinacyanol in methanol at RT is shown in grey. The χ^2 for the global fitting was 1.14. (d) Average lifetime of fluorescence time traces (calculated as $\tau_{avg} = (\sum_k A_k \tau_k)/\sum_k A_k$, where A_k is the positive amplitude of the component associated with the lifetime τ_k, and k = 1 to 3) at different wavelengths. The black data points are obtained from the presented 77 K data, whereas the red data points are calculated from the RT data in Mascoli et al.[1].

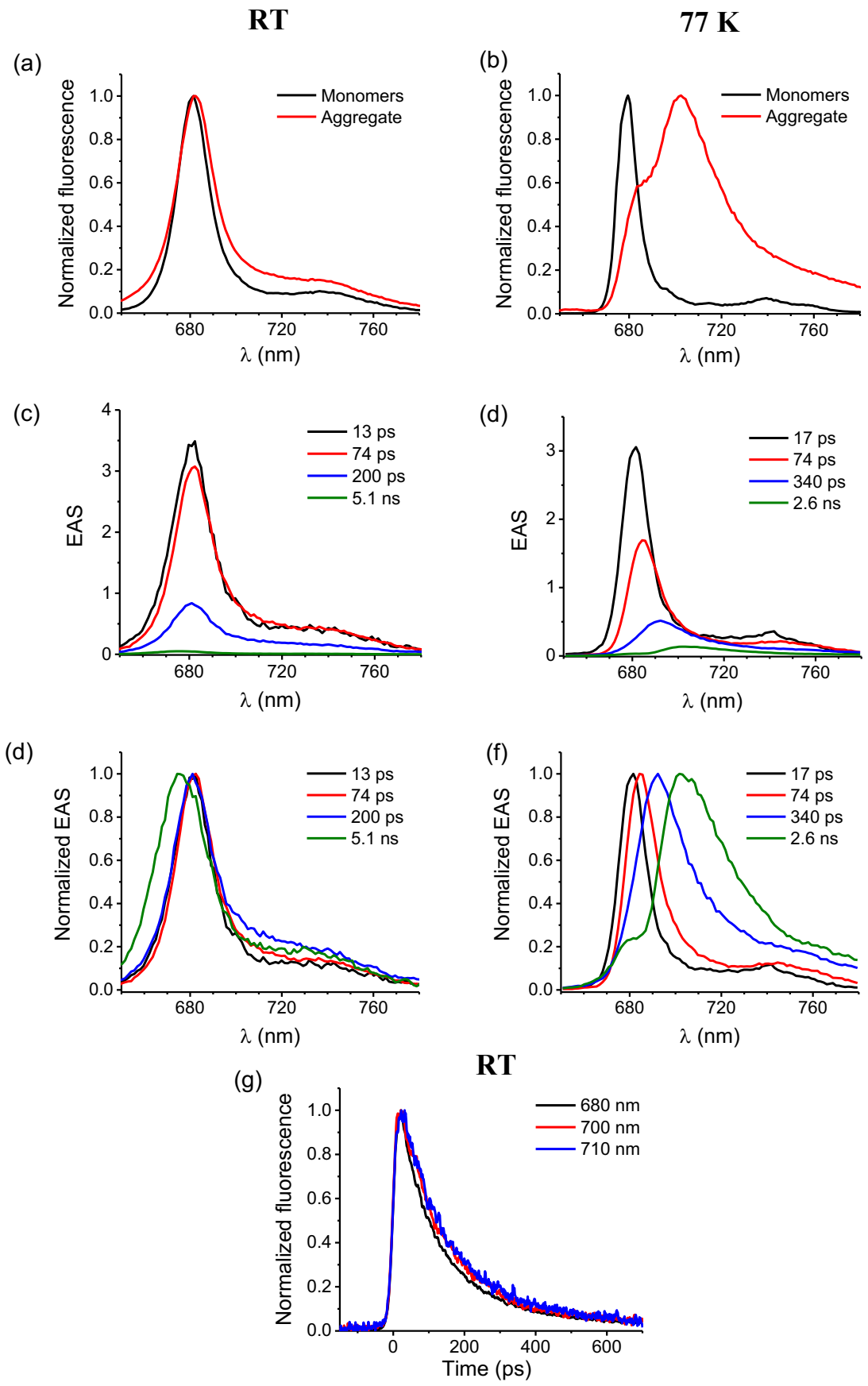
RT
77 K
(a)
(b)
Monomers
Aggregate
Normalized fluorescence
λ (nm)
(c)
(d)
13 ps
74 ps
200 ps
5.1 ns
17 ps
340 ps
2.6 ns
EAS
(d)
(f)
Normalized EAS
(g)
680 nm
700 nm
710 nm
Time (ps)

Figure S4. Fluorescence measurements of CP29 oligomers. (a) Overlay of the steady-state fluorescence spectra of CP29 aggregates and monomers excited at 470 nm at RT. (b) Overlay of the steady-state fluorescence spectra of CP29 aggregates and monomers excited at 470 nm at 77 K. (c) Evolution-Associated Spectra (EAS) resulting from a sequential kinetic analysis of the RT time-resolved data in Figure 2a (see DAS in Figure 2b for the corresponding parallel kinetic scheme). (d) Evolution-Associated Spectra (EAS) resulting from a sequential kinetic analysis of the 77-K data in Figure 3a (see DAS in Figure 3d for the corresponding parallel kinetic scheme). The corresponding normalized EAS are shown in (e) and (f). (g) Normalized TRF traces of CP29 WT oligomers at RT detected at different wavelengths.

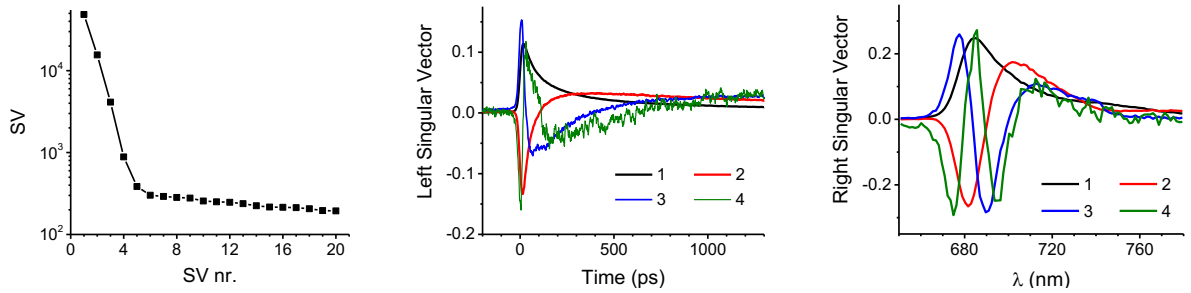

Figure S5. Singular Value Decomposition (SVD) of the time-resolved fluorescence data of CP29 oligomers at 77 K depicted in Figure 3a. By SVD, the time and wavelength dependent fluorescence data F(λ,t) can be decomposed as:

$$\mathbf{F(\lambda, t) = \sum_k SV_k \cdot P_k(t) \cdot S_k(\lambda)} \qquad \text{[Equation S1]}$$

Where $P_k(t)$ (central panel) and $S_k(t)$ (right panel) represent a concentration time profile and a spectrum for the *k*th contribution, and the singular value (SV, left panel) is a positive number determining the weight of the *k*th [P(t)·S(λ)] contribution to the total decomposition. The SVs contribute to the summation in the decreasing order. The final spectra $SAS_k(\lambda)$ and population profiles $C_k(t)$ used in the manuscript (and shown, for instance, in Figure 4a-b for the data of CP29 WT oligomers at 77 K) are obtained from linear combinations of the spectra $S_k(\lambda)$ and the SV-scaled concentration profiles $[SV_k \cdot P_k(t)]$ from the SVD. Here, SVD reveals four linearly independent components distinct from noise and with sharply decreasing weight (the noise level is represented by the plateau in the SV-plot), whose kinetic profiles and spectra are depicted in the central and right panels. The first three components, however, were enough to reproduce the data with good accuracy (see Figure S6), and were therefore linearly combined to obtain the three spectra and kinetic profiles displayed in Figure 4a-b.

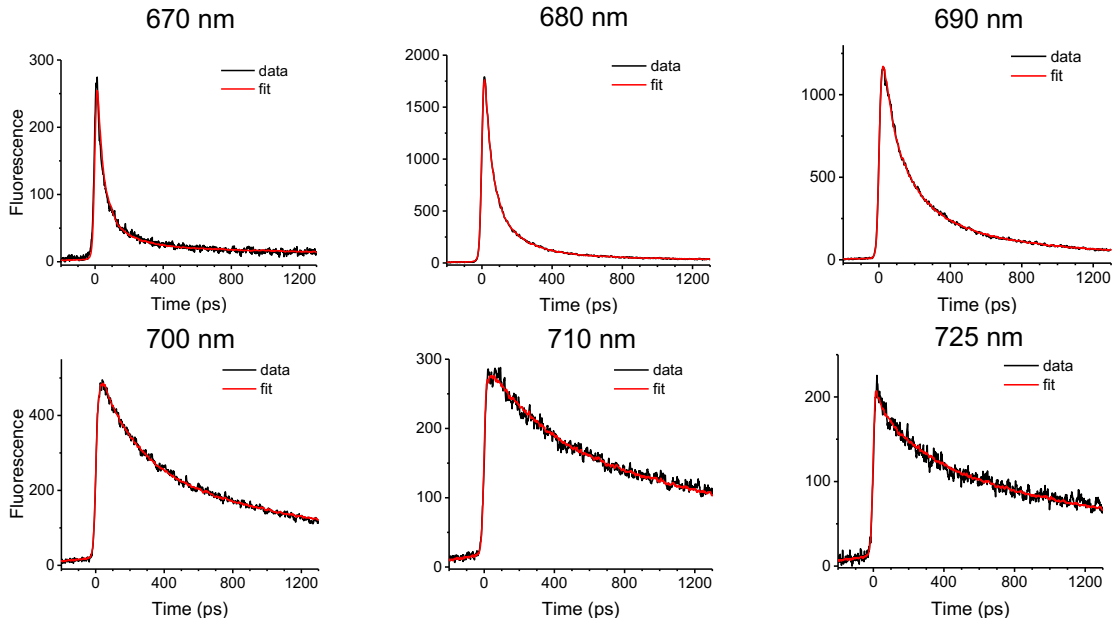

Figure S6. Analysis of time-resolved fluorescence data of CP29 oligomers at 77 K. Overlay of the experimental data (black lines) and the data reconstructed (red lines) using the first three components from the SVD shown in Figure S5 (i.e. by truncating the summation in Equation S1 after the third term) at different emission wavelengths. The fitted traces can also be obtained by summing the contributions from all three spectral components ($SAS_k(\lambda)$) and population profiles $C_k(t)$ shown in Figure 4a-b.

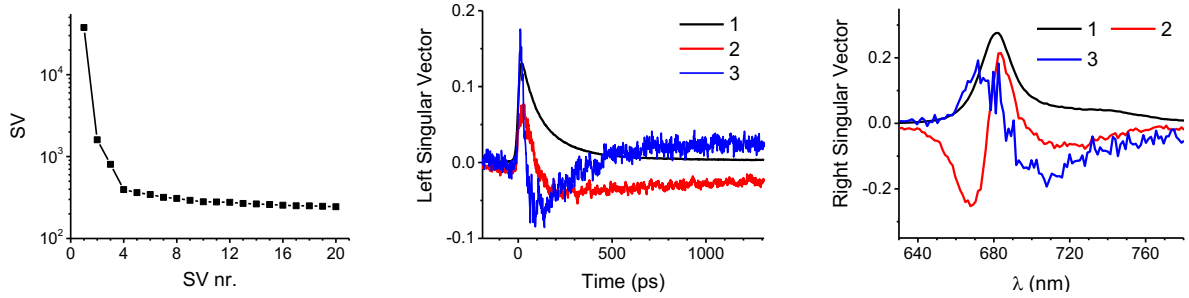

Figure S7. SVD of the time-resolved fluorescence data of CP29 WT at RT (Figure 2a). SVs are shown on the left in decreasing order, with their related kinetic profiles and spectra in the central and right panel, respectively (see Figure S5 for details). SVD reveals the presence of three components above the noise level, which were combined to yield the spectra $SAS_k(\lambda)$ and kinetic profiles $C_k(t)$ in Figure 4d-e. The first SV is much larger than the two following ones, meaning that the kinetics is dominated by the first of the three components (resulting in the blue SAS and kinetic traces of Figure 4d-e).

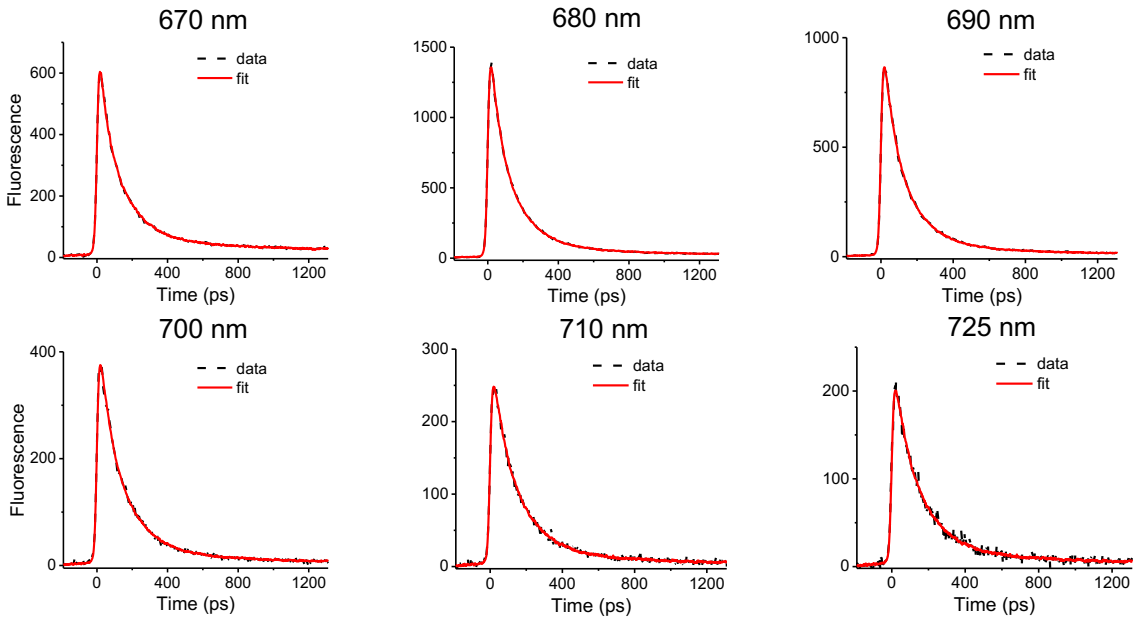

Figure S8. Analysis of time-resolved fluorescence data of CP29 oligomers at RT. Overlay of the experimental data (black lines) and the data reconstructed (red lines) using the first three components from the SVD shown in Figure S7 at different emission wavelengths. The fitted traces can also be obtained by summing the contributions from all three spectral components ($SAS_k(\lambda)$) and population profiles $C_k(t)$ shown in Figure 4d-e.

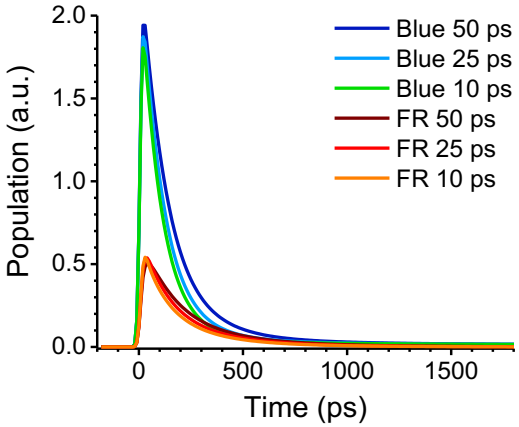

Figure S9. Simulated kinetics of Blue and FR components from CP29 WT aggregates at RT with different inter-complex hopping times. The curves were simulated by using the same fitting parameters listed in Table 1 in the manuscript but changing the hopping time between isoenergetic complexes from 25 ps (as in Figure 4e) to either 10 ps or 50 ps. All other hopping times were also rescaled to maintain the same relative excited state free energies between different fluorescent states.

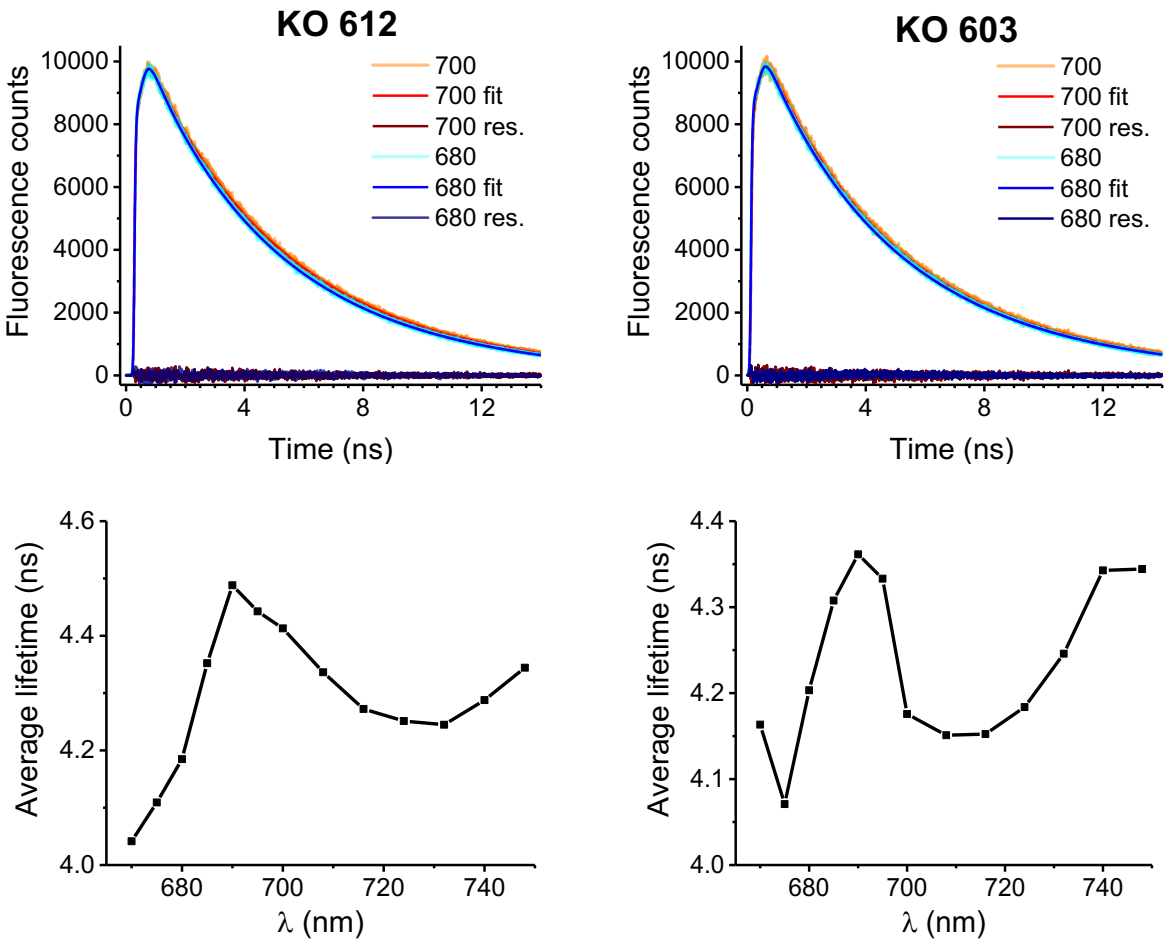

Figure S10. Time-resolved fluorescence experiments of CP29 KO monomers at 77 K (compare to Figure S3). Upper panels show measured (in transparent cyan/orange) and globally fitted (in blue/red) fluorescence time traces at 680 nm and 700 nm for CP29 KO612 (left) and KO603 (right) at 77 K upon 468 nm excitation. Experimental traces are scaled to the same maximum. The difference between measured and fitted data (residuals) is displayed in black/violet. The χ^2 for the global fitting was 1.07 (1.09) for CP29 KO612 (KO603). Lower panels show the average lifetime of fluorescence time traces at different wavelengths (see caption of Figure S3 for details about the calculation). The average lifetimes of both KO complexes exhibit some wavelength dependency, rising above 680 nm and peaking at 690 nm (instead of 700 nm as in the WT, *cf.* Figure S3). The wavelength-dependence is also less-pronounced in comparison to the WT complexes, especially for the KO603 one, suggesting that a smaller number of red-emitting complexes might exist in the ensemble.

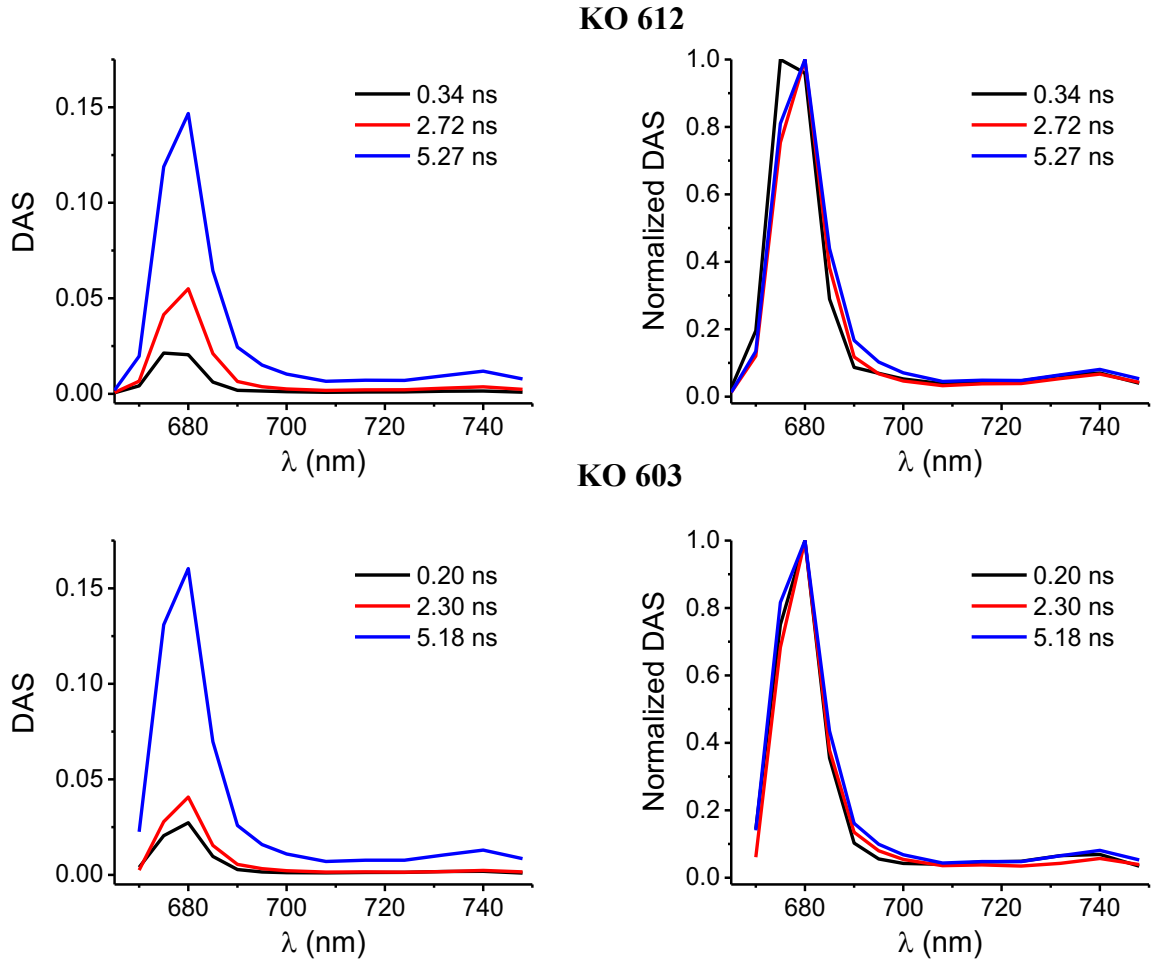

Figure S11. DAS (left) and normalized DAS (right) from global analysis of time-resolved fluorescence data of CP29 KO612 (left) and KO603 (right) monomers at 77 K upon 468 nm excitation (see also Figure S3 and S10). In both mutants, three lifetime components can be resolved, representing distinct emissive states of the complexes in the ensemble. Again, the majority of complexes can be found in a long-lived state (with lifetimes longer than 5 ns), whereas smaller subpopulations are found in slightly quenched (> 2 ns) and strongly quenched (< 0.5 ns) states. For CP29 KO612 (KO603), the relative amplitudes of the different components at 680 nm are 66% (70%) for the long-lived component, 25% (18%) for the intermediate component and 9% (12%) for the short-lived component. These lifetimes and amplitudes are comparable to those observed at RT[1], as already discussed for the WT antenna. In both mutant complexes, the fastest lifetime component displays less amplitude in the region around 700 nm, indicating that the red-emitting complexes are mostly unquenched, as for CP29 WT.

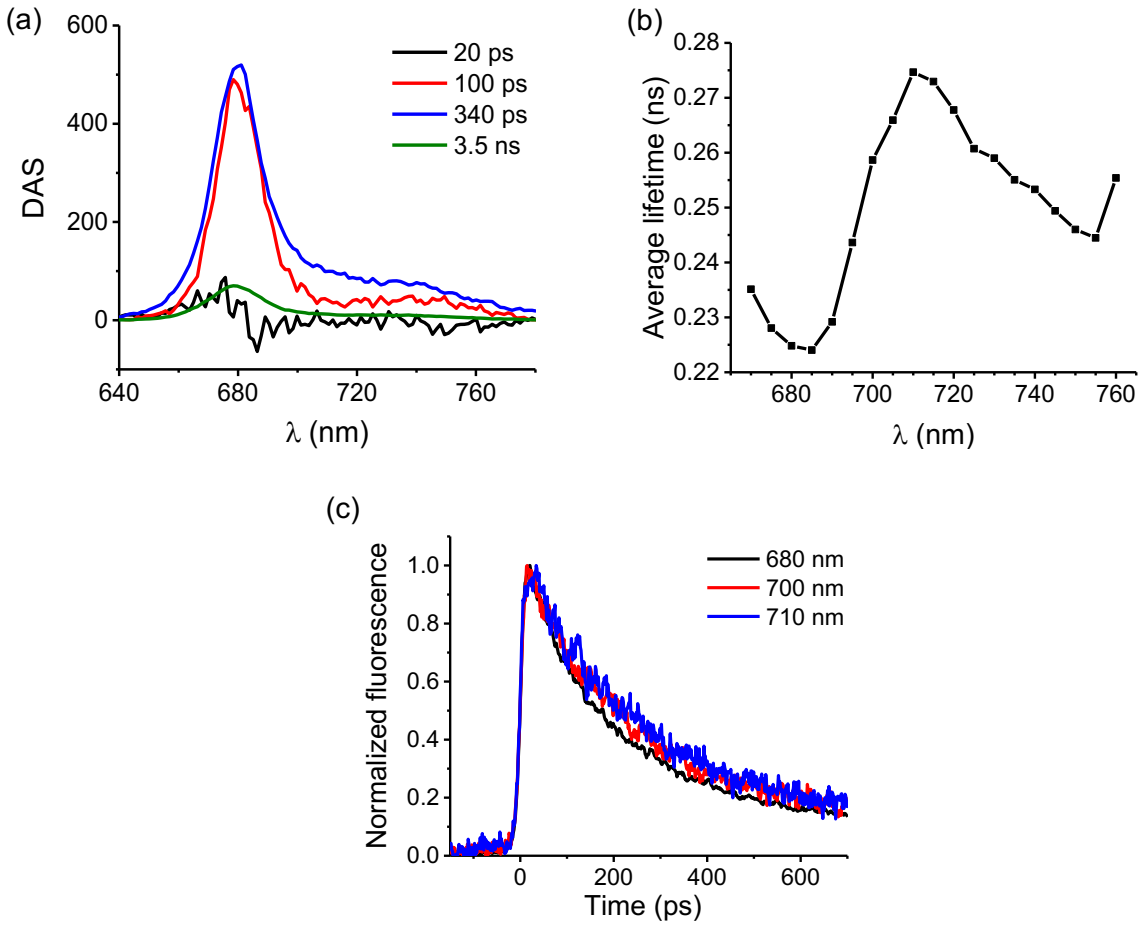

Figure S12. Time-resolved fluorescence of CP29 KO612 oligomers at RT. (a) DAS from global analysis of the fluorescence data. (b) Average Chl excited state lifetime at different wavelengths. Only the 100-ps and the 340-ps components, representing excited state relaxation in the aggregate, were used for the average (see caption of Figure 2 in the main text for further details). The DAS and the average lifetime show the same trends observed for CP29 WT (see Figure 2 and the results section in the manuscript), even though the overall quenching is (nearly twice) slower for the KO612 mutant oligomers. Note that a larger number of unconnected antennae is present in this sample (as witnessed by the larger amplitude of the long-lived component, peaking slightly below 680 nm). However, its contribution to the average lifetime is not included in the plot on the right panel. The standard deviation on the average lifetime is ±7 ps. (c) Normalized TRF traces of CP29 KO612 oligomers at RT detected at different wavelengths.

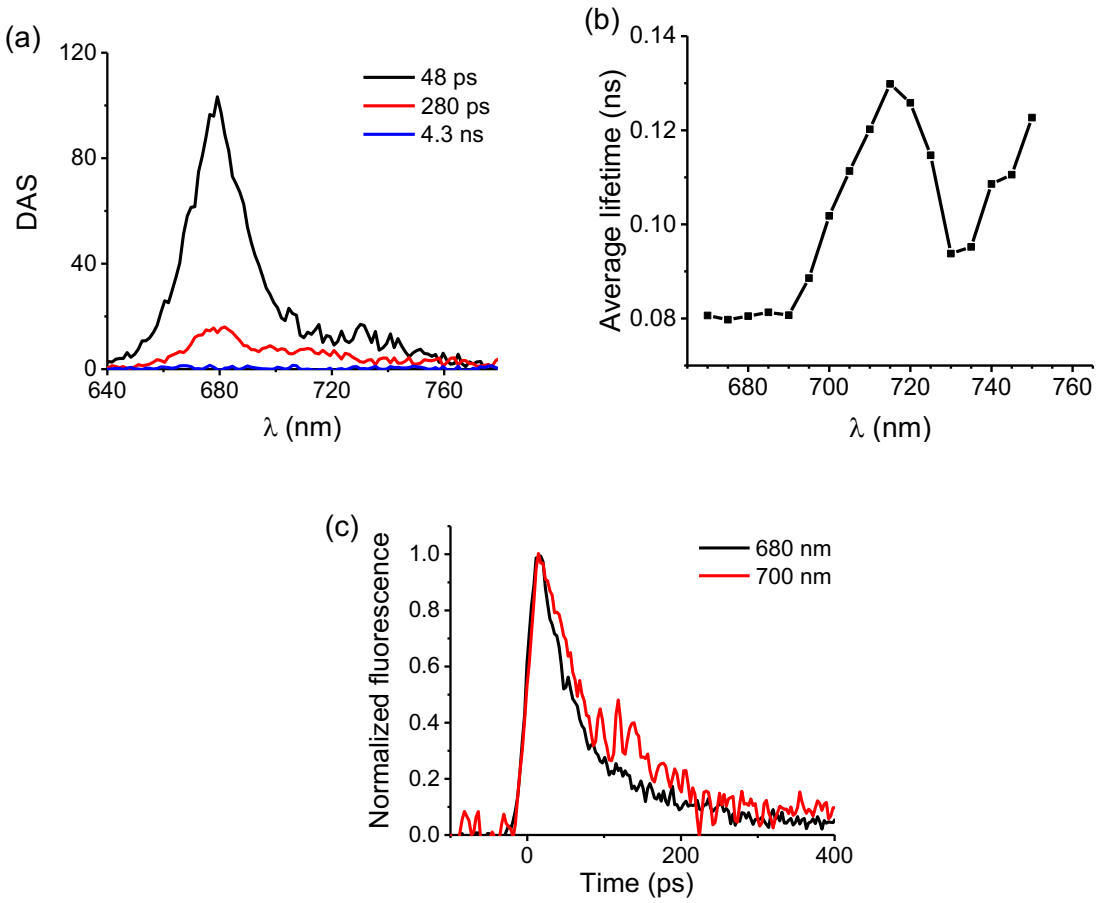

Figure S13. Time-resolved fluorescence of CP29 KO603 oligomers at RT. (a) DAS from global analysis of the fluorescence data. (b) Average Chl excited state lifetime at different wavelengths. Only the 48-ps and the 280-ps components, representing excited state relaxation in the aggregate, were used for the average (see main text and the caption of Figure 2 for further details). The DAS and the average lifetime show the same trends observed for CP29 WT (see Figure 2 and the results section in the manuscript), even though the overall quenching is (slightly) faster for the KO603 mutant oligomers. The standard deviation on the average lifetime is ±10 ps. (c) Normalized TRF traces of CP29 KO603 oligomers at RT detected at different wavelengths.

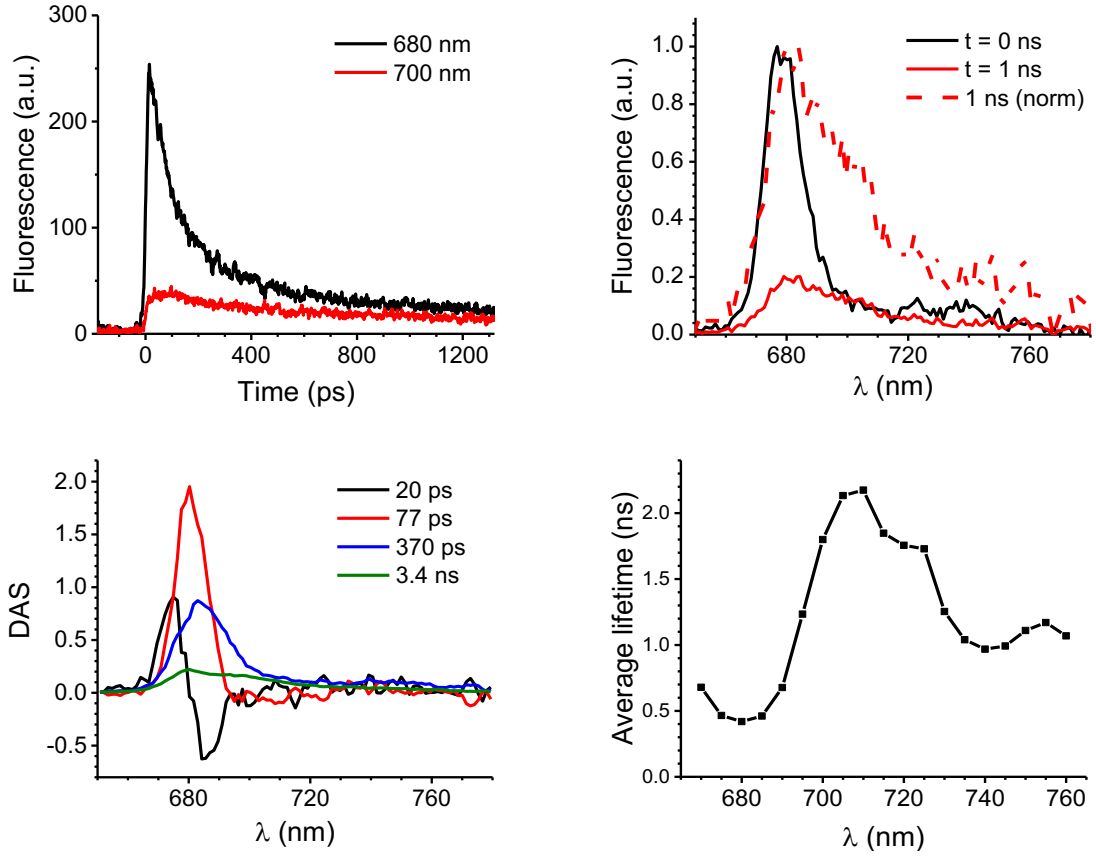

Figure S14. Time-resolved fluorescence of CP29 KO612 oligomers at 77 K. Top left: time traces at 680 nm (black) and 700 nm (red). Top right: fluorescence spectra immediately after excitation (black) and 1 ns after (solid red, and normalized in dashed red). Bottom left: DAS from global analysis of the fluorescence data. Bottom right: average Chl excited state lifetime at different wavelengths. The fastest component, representing mostly downhill energy transfer, was excluded from the average (see main text and Figure 3 for details). Note that both the DAS and the average lifetimes show the same trends observed for CP29 WT aggregates (Figure 3). However, the overall quenching is significantly slower. In addition, the small number of unconnected antennae already observed in the RT experiment (see Figure S12 and the green DAS in the bottom-left figure, which has similar amplitude at 680 and 700 nm) influences the calculated lifetime in the bottom-right plot. Indeed, to account for the contribution from the red-emitting states in the aggregate (which decay in nanoseconds at 77 K), the longer-lived component was also included in the average lifetime calculation. In this case, the fitting resulting from MCR is essential to disentangle the contribution from long-lived red-emitting states and that from uncoupled antennae (see Figure S20).

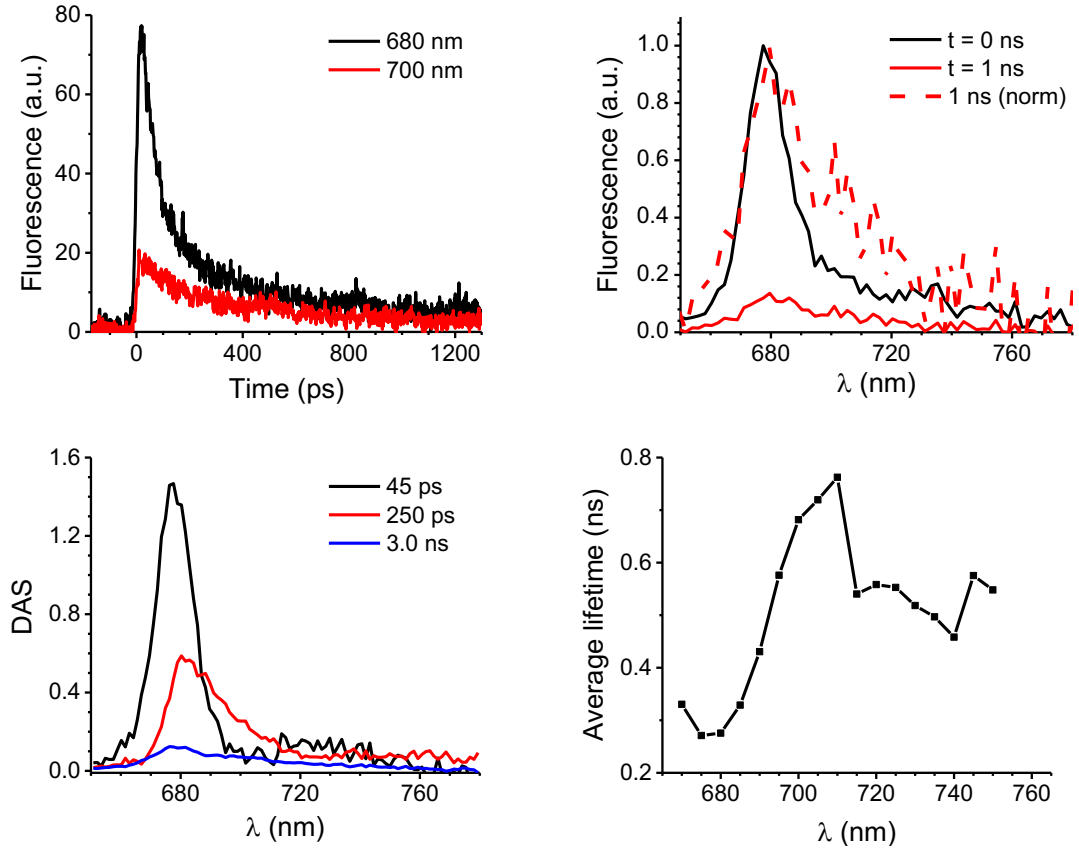

Figure S15. Time-resolved fluorescence of CP29 KO603 oligomers at 77 K. Top left: selected time traces at 680 nm (black) and 700 nm (red). Top right: fluorescence spectra immediately after excitation (black) and 1 ns after (solid red, and normalized in dashed red). Bottom left: DAS from global analysis of the fluorescence data. Bottom right: average Chl excited state lifetime at different wavelengths (see main text and Figure 3 for details). Note that both the DAS and the average lifetimes show similar trends to those observed for CP29 WT aggregates (even though one less DAS could be resolved in this case). The average lifetime increases in the far-red region, but not as much as it was observed in the other samples. This can be explained with the amount of long-lived red emission decreasing significantly (see blue DAS in the bottom-left panel: the contribution from red-emitting states is nearly half of that from the minor fraction of unconnected antennae). At the same time, the lifetimes of the black and red DAS, representing excited state decay processes, are shorter than in CP29 WT (and KO612) oligomers, suggesting that quenching is faster in the KO603 oligomers (as confirmed by the model-based fitting results, see following figures). Again, MCR helps disentangling the contributions from unconnected antennae and from long-lived redshifted states (see Figure S21).

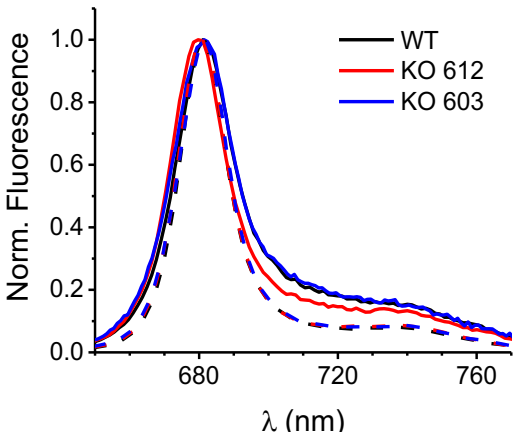

Figure S16. Solid lines: time-integrated fluorescence spectra of CP29 (WT and KO mutants) oligomers at RT (see Figures 2, S12 and S13 for the time-resolved data). The small nanosecond components representing contributions from detached antennas and uncoupled pigments were excluded from the integration to extract the steady state spectrum of the aggregate only. For CP29 KO603 oligomers, the long-lived contribution was difficult to estimate (due to the lower signal-to-noise ratio) and the steady state emission upon 500 nm excitation is shown instead. Dashed lines: steady-state fluorescence spectra of CP29 (WT and KO mutants, 500 nm excitation) monomers at RT. The lower amount of red-emission is evident in the KO612 aggregates, whereas the KO603 and WT aggregates have overlapping spectra. The smaller amount of red-emitting species is the KO603 aggregate at RT is clearer from the fitting of MCR traces (see Table S2).

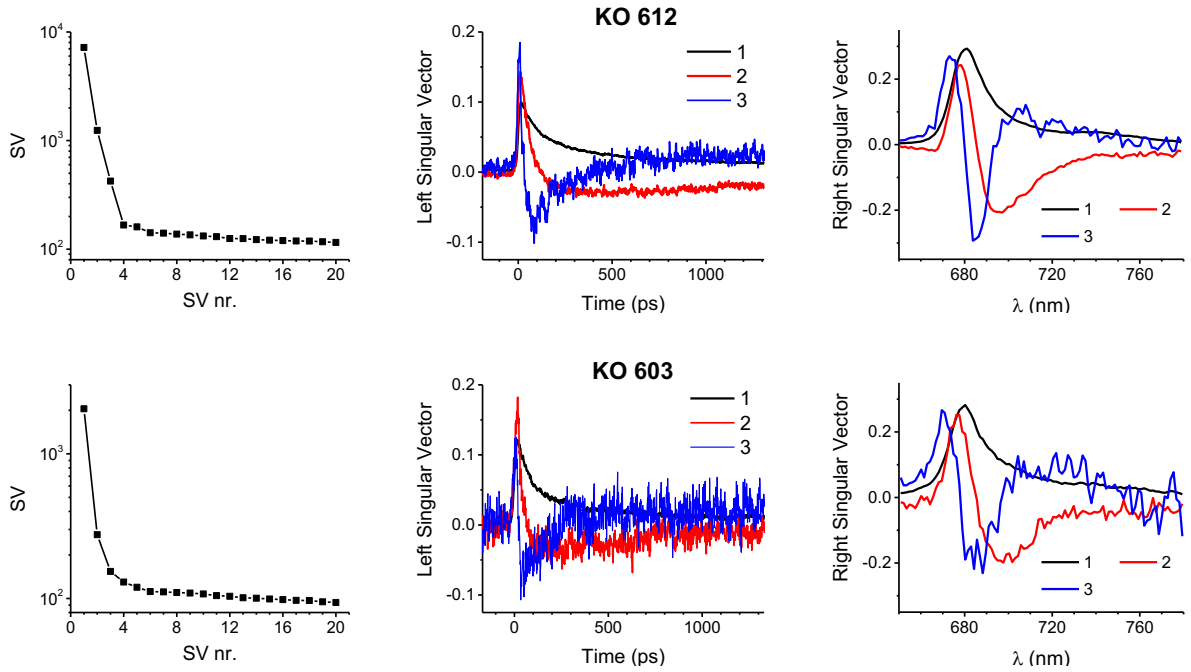

Figure S17. SVD of the time-resolved fluorescence data of CP29 KO612 (top) and KO603 (bottom) at 77 K (see Figure S5 for details about SVD and Figures S14-15 for the DAS from global analysis). SVs are shown on the left in decreasing order, with their related kinetic profiles and spectra in the central and right panel, respectively. SVD reveals the presence of three components above the noise level, which were combined to yield the spectra $SAS_k(\lambda)$ and kinetic profiles $C_k(t)$ in Figures S20-21. Note that the overall profiles of left and right singular vectors are very similar in the different samples (though with different noise levels, see also Figure S5 for CP29 WT), suggesting that a common model (with possible changes in the precise timescales and/or amplitude of certain components) can in principle describe all data.

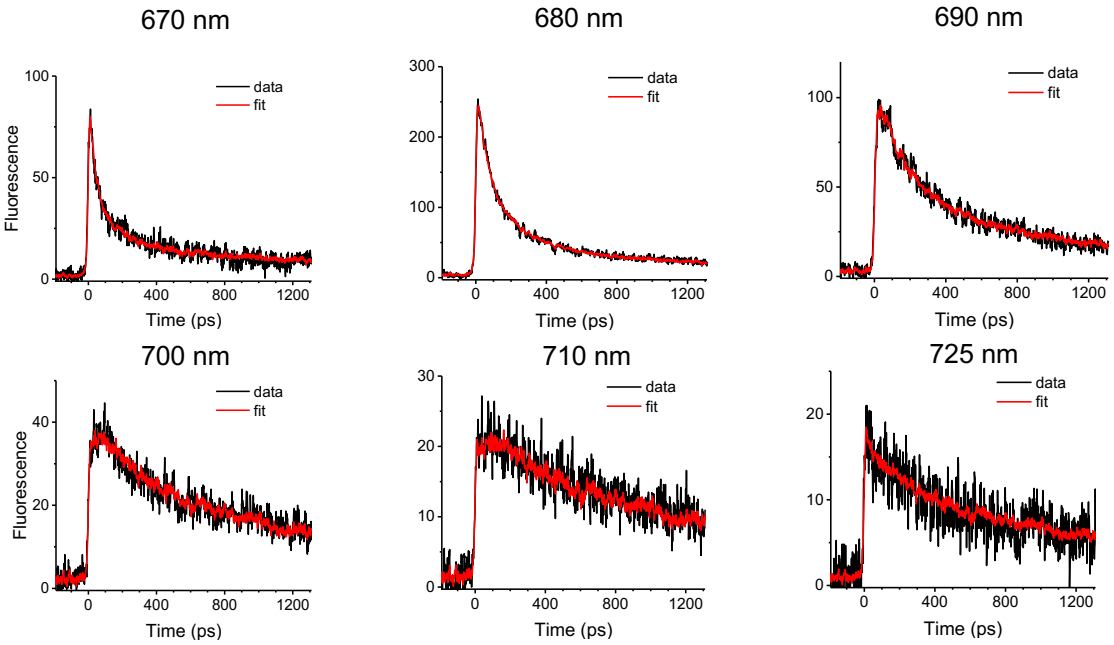

Figure S18. Analysis of time-resolved fluorescence data of CP29 KO612 oligomers at 77 K. Overlay of the experimental data (black lines) and the data reconstructed (red lines) using the first three components from the SVD shown in Figure S17 at different emission wavelengths. The fitted traces can also be obtained by summing the contributions from all three spectral components $SAS_k(\lambda)$ and kinetic profiles $C_k(t)$ shown in Figure S20.

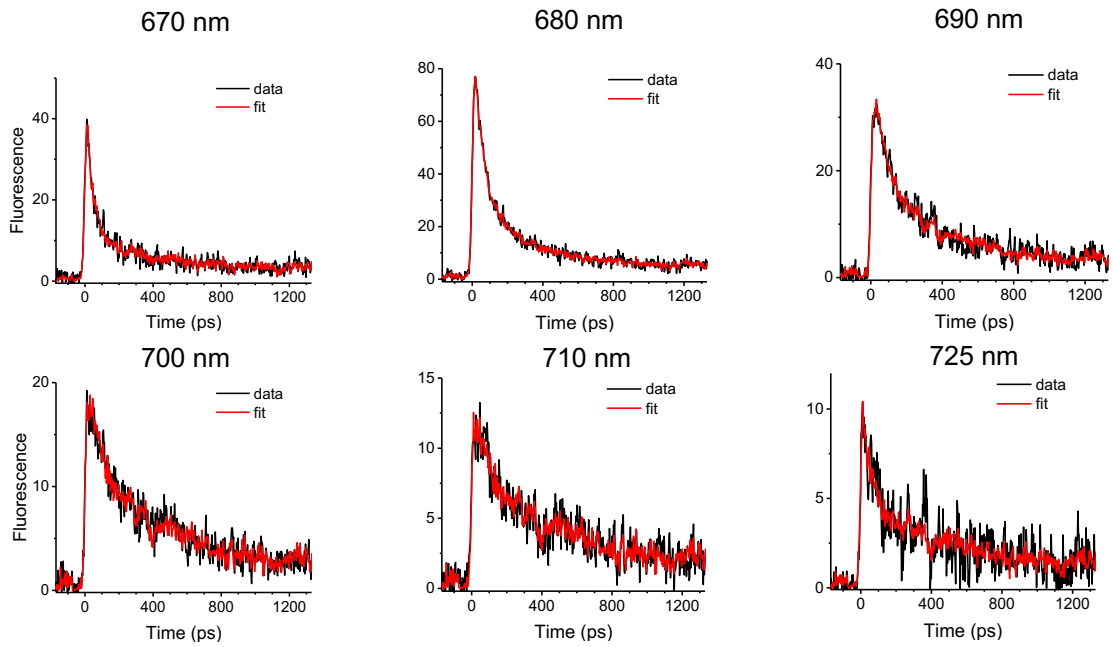

Figure S19. Analysis of time-resolved fluorescence data of CP29 KO603 oligomers at 77 K. Overlay of the experimental data (black lines) and the data reconstructed (red lines) using the first three components from the SVD shown in Figure S17 at different emission wavelengths. The fitted traces can also be obtained by summing the contributions from all three spectral components $SAS_k(\lambda)$ and kinetic profiles $C_k(t)$ shown in Figure S21.

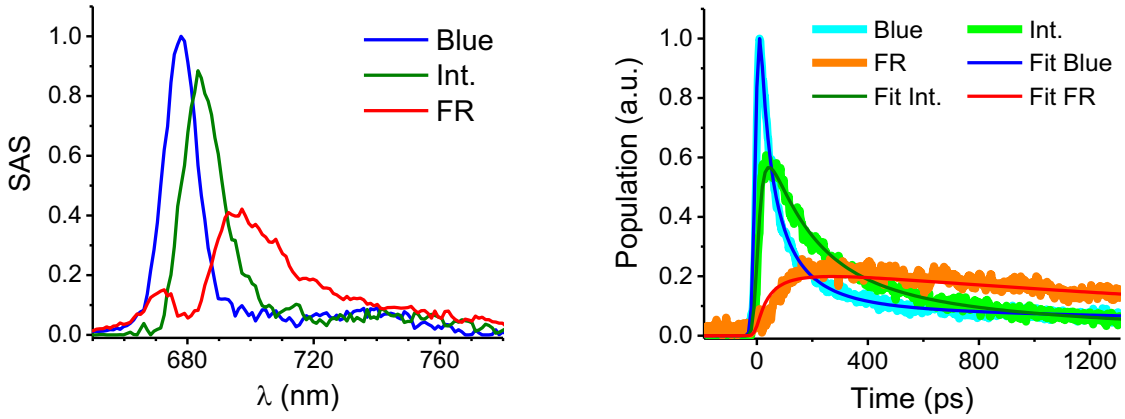

Figure S20. SAS (normalized to their area) of the three components from MCR of fluorescence data of CP29 KO612 oligomers at 77 K (left) and kinetic traces associated to each SAS (right). The traces obtained from MCR are presented in thick lines, whereas those fitted based on the heterogeneous model discussed in the manuscript are presented in thin solid lines. Note that the smaller short-wavelength contribution (peaking near 670 nm) to the red SAS is due to a small amount of long-lived unconnected pigments, which is difficult to separate from the contribution of long-lived red-emitting states present in the aggregate. The spectrum of the blue component peaks at 678 nm, closely matching the 77 K emission of KO612 monomers (peaking at 678.5 nm). The spectrum of the FR component peaks below 700 nm and is therefore blue-shifted compared to the 700-nm SAS in oligomeric CP29 WT. The intermediate component also blue-shifts (the maximum being at 684 rather than 688 nm). The parameters obtained from the fitting are presented in Table S1 and reveal that the number of quenched KO612 complexes doubles and their trapping is significantly faster upon aggregation. On the other hand, the amount of FR complexes decreases from 3.8% in the WT oligomers (see Table 1 in the manuscript) to 1.8% in the KO612 oligomers (a trend which is also reproduced at RT, see Table S1 and Figure S25).

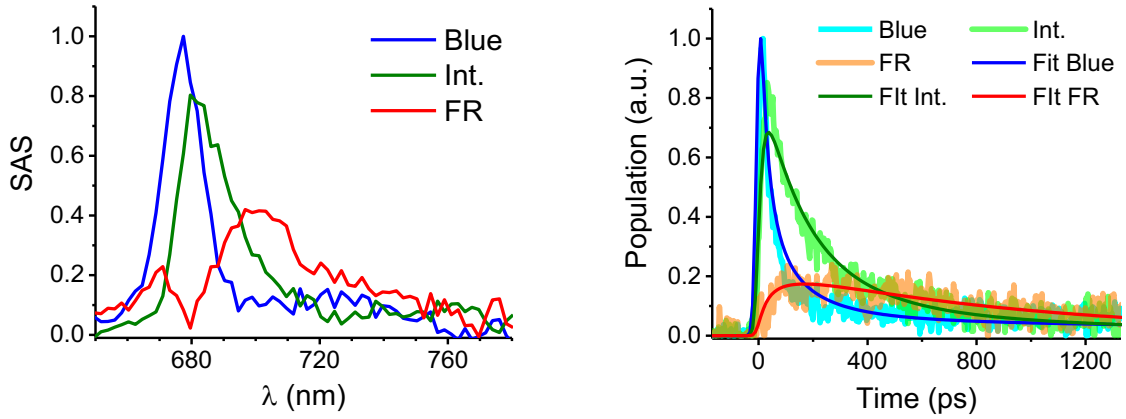

Figure S21. SAS (normalized to their area) of the three components from MCR of fluorescence data of CP29 KO603 oligomers at 77 K (left) and kinetic traces associated to each SAS (right). The traces obtained from MCR are presented in thick lines, whereas those fitted based on the heterogeneous model discussed in the manuscript are presented in thin solid lines. Note that the smaller short-wavelength contribution in the red SAS (peaking at 670 nm) is due to a small amount of long-lived unconnected pigments, which is difficult to separate from the contribution of long-lived red-emitting states present in the aggregate (see also Figure S20). The maxima of the blue and intermediate SAS are very close (with the intermediate component approaching 680 nm), even though their spectral broadening is different. This effect might result from a narrower distribution of redshifted spectral forms inside KO603 oligomers in comparison to the CP29 WT ones. The fitting parameters are shown in Table S2. Due to the lower signal-to noise ratio of the KO603 data (see SVD in Figure S17 and raw data in Figure S19), the estimation of the lifetime of quenched complexes is affected by a larger error, as a similar fitting quality was achieved when this parameter was varied between 30 and 50 ps. The values in Table S2 were obtained by setting the lifetime of quenched complexes to 50 ps. These data demonstrate that the number of quenched complexes significantly increases upon oligomerization of KO603 CP29. In addition, the amount of strongly redshifted complexes (1.6%) is less than half of what found for CP29 WT oligomers (3.8%).

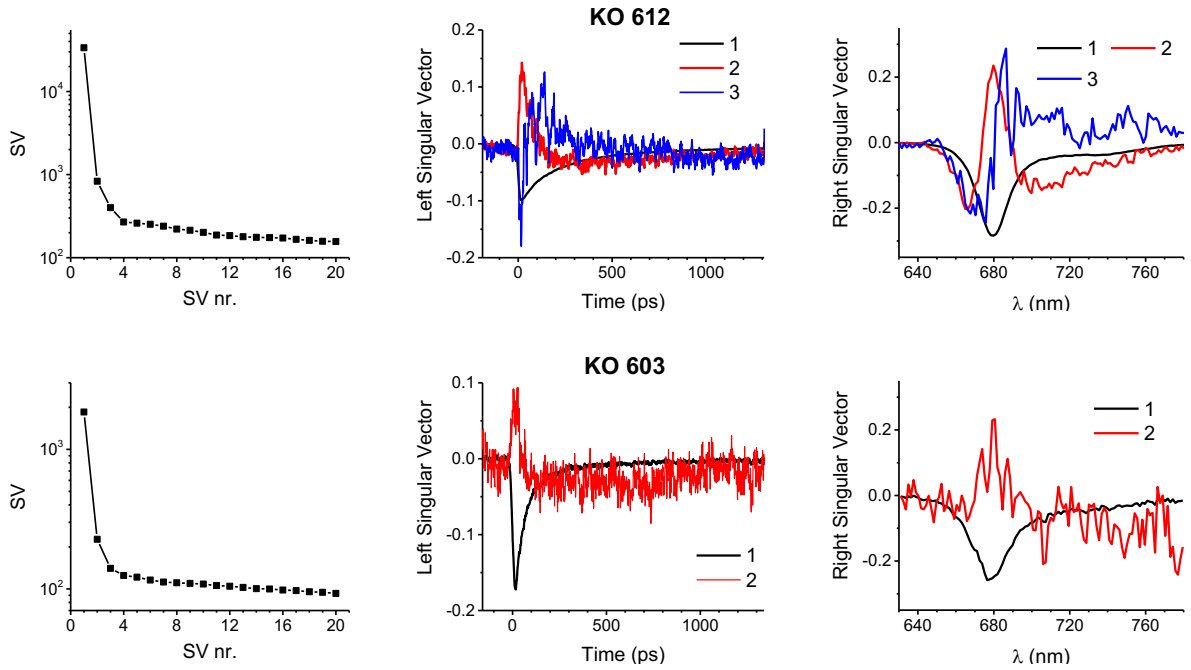

Figure S22. SVD of the time-resolved fluorescence data of CP29 KO612 (top) and KO603 (bottom) at RT (see Figure S5 for details about SVD and Figures S12-13 for the DAS from global analysis). SVs are shown on the left in decreasing order, with their related kinetic profiles and spectra in the central and right panel, respectively. SVD reveals the presence of three components (two in the case of CP29 KO603) above the noise level, which were combined to yield the spectra $SAS_k(\lambda)$ and kinetic profiles $C_k(t)$ in Figures S25-26.

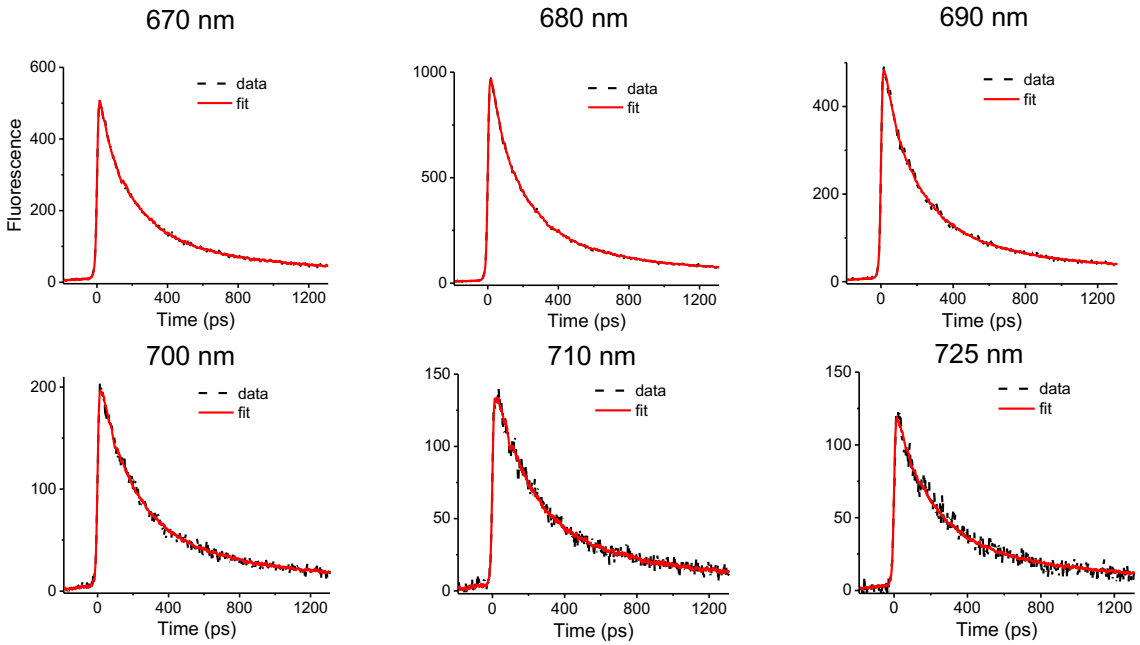

Figure S23. Analysis of time-resolved fluorescence data of CP29 KO612 oligomers at RT. Overlay of the experimental data (black lines) and the data reconstructed (red lines) using the first three components from the SVD shown in Figure S22 at different emission wavelengths. The fitted traces can also be obtained by summing the contributions from all three spectral components $SAS_k(\lambda)$ and kinetic profiles $C_k(t)$ shown in Figure S25.

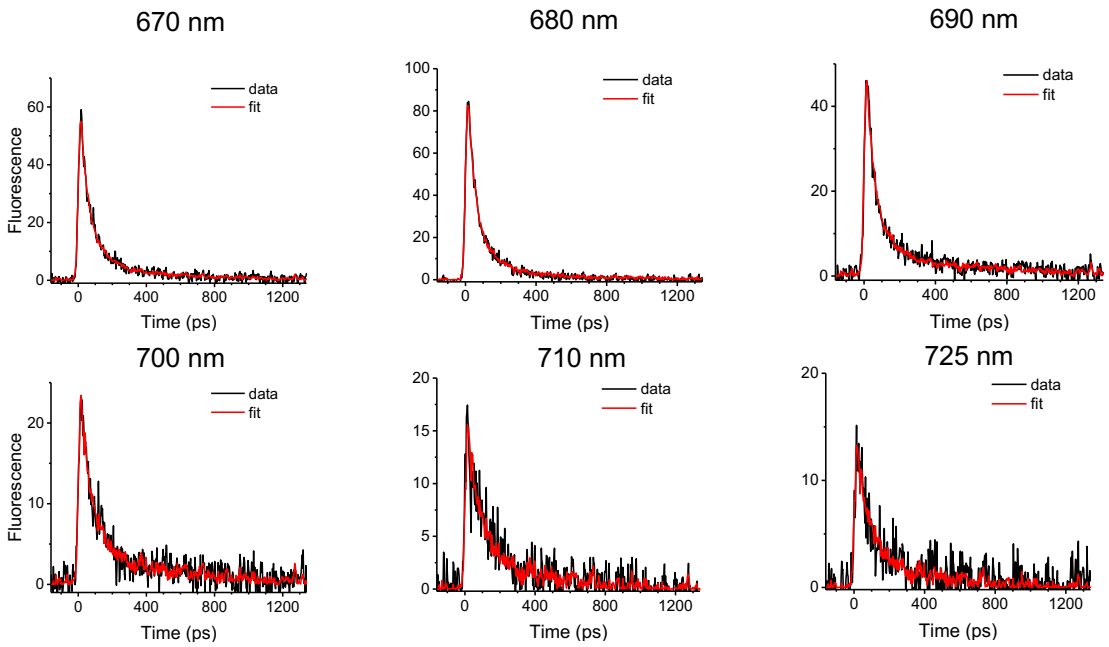

Figure S24. Analysis of time-resolved fluorescence data of CP29 KO603 oligomers at RT. Overlay of the experimental data (black lines) and the data reconstructed (red lines) using the first two components from the SVD shown in Figure S22 at different emission wavelengths. The fitted traces can also be obtained by summing the contributions from the two spectral components $SAS_k(\lambda)$ and kinetic profiles $C_k(t)$ shown in Figure S26.

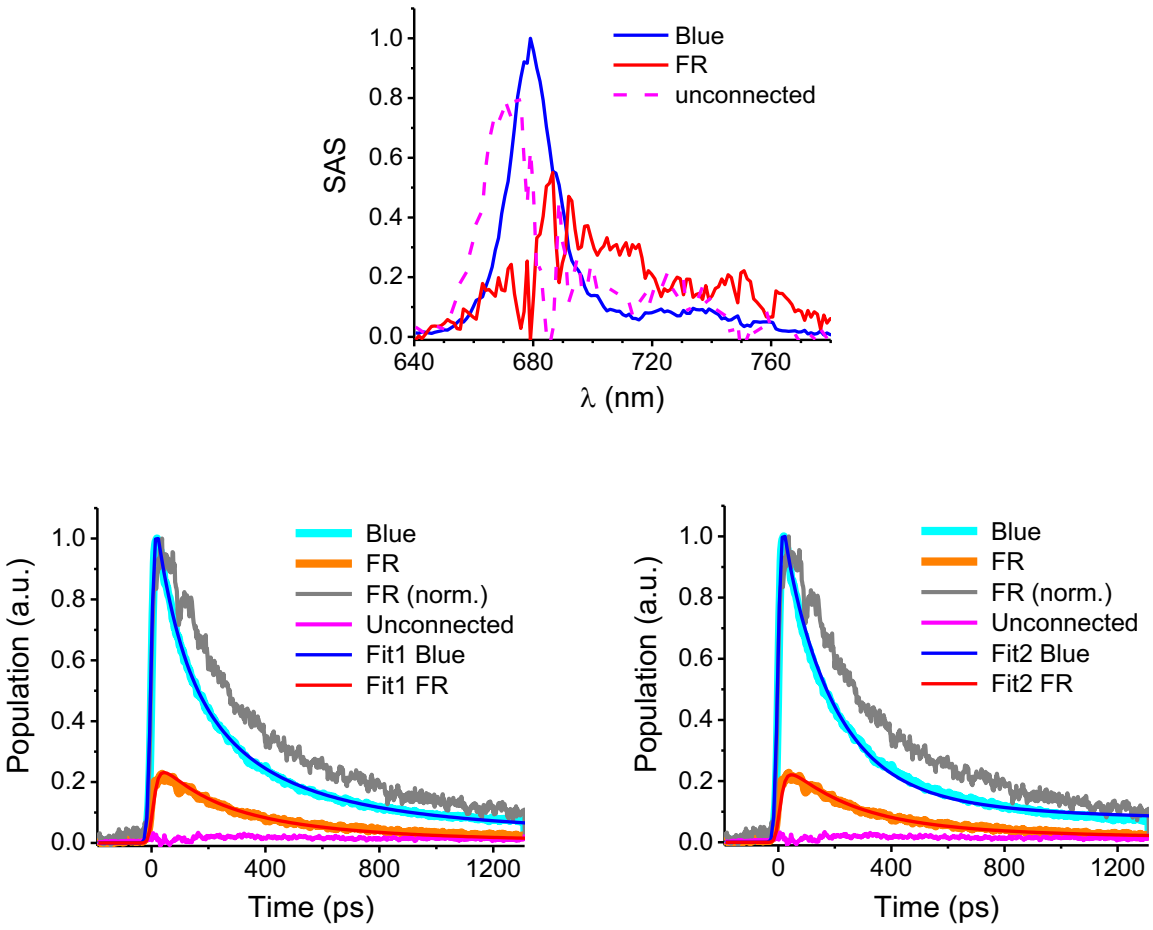

Figure S25. SAS (normalized to their area) of the three components from MCR of fluorescence data of CP29 KO612 oligomers at RT (top) and kinetic traces associated to each SAS (bottom left and right) according to two distinct set of parameters found via our evolutionary research algorithm. The traces obtained from MCR are presented in thick lines, whereas those fitted based on the heterogeneous model discussed in the manuscript are presented in thin solid lines. The three SAS are comparable to those observed in the WT oligomers and represent blue complexes, FR complexes and a small amount of long-lived unconnected pigments respectively (the separation of the red and magenta components is not as good as for the WT data due to the smaller amounts of both red forms and uncoupled pigments). Note that the blue component does not entirely decay during the experimental time window due to a small amount of long-lived unconnected antennae (see the last column of Table S1 for the amount estimated from the fitting). For this dataset, two distinct parameter configurations were found yielding reasonable fitting quality (see model 1 and 2 in Table S1). These fitting solutions predict similar parameters for the red-emitting states (whose amount is consistently reduced in comparison to the WT oligomers, both at RT and 77 K), but rather distinct parameters for the quenched complexes. Model 1 (fitted traces are shown in the bottom left panel) predicts a smaller amount (around 5%) of strongly quenched complexes ($\tau < 50$ ps) and yields the best overall fitting, especially for the 680-nm component, representing the largest part of the signal. Model 2 (fitted traces are shown in the bottom right panel) predicts instead a larger number (around 30%) of slower quenchers ($\tau > 150$

ps). This model results in an overall worse fitting quality, even though the trace of the red-emitting species is better fitted. Based on the results from monomeric CP29 KO612, it is difficult to state which model is more reliable. Indeed, if for CP29 WT, aggregation did not change substantially the relative amount and the trapping rate of quenched complexes, the same trend does not hold for the KO612 oligomers. According to model 1, the amount of quenchers, which is comparatively low in the monomers, remains relatively small in the oligomers, but their trapping lifetime decreases by a factor of six. Model 2 represents the other extreme, where the lifetime of the quenchers is almost not affected by oligomerization, whereas their amount substantially increases. Both models predict, therefore, a significant change in the properties of the quenched state upon oligomerization (either its occurrence or its trapping rate).

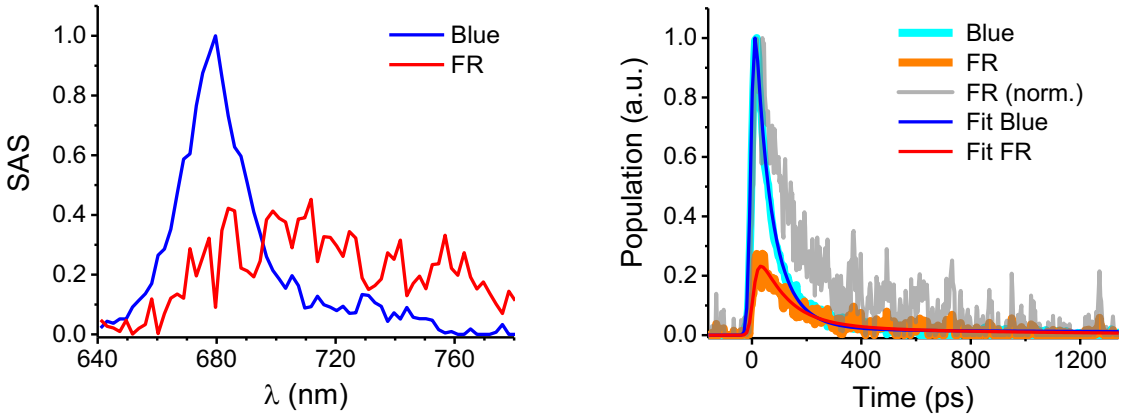

Figure S26. SAS (normalized to their area) of the two components from MCR of fluorescence data of CP29 KO603 oligomers at RT (top left) and kinetic traces associated to each SAS. The traces obtained from MCR are presented in thick dashed lines, whereas those fitted based on the heterogeneous model discussed in the manuscript are presented in thin solid lines. The two SAS are comparable to those observed in the WT oligomers and represent 680-nm complexes and red-emitting complexes. Due to the much lower sample concentration and the resulting worse signal-to-noise ratio, the extraction of the red component was not as effective as for the other samples, but its spectral and kinetic signatures are consistent with those from CP29 WT and KO612. Due to the lower data quality, the estimation of the lifetime of the quenched complexes is also affected by a larger error, as a similar fitting quality was achieved when this parameter was varied between 30 and 50 ps. The parameters shown in Table S2 were obtained when the lifetime of quenched complexes was fixed to 50 ps, which is rather similar to that of quenched isolated complexes at RT. The parameters listed in Table S2 reveal that the number of red-emitting complexes in the aggregate decreases in comparison to what previously observed for CP29 WT (consistent with the results from the 77 K data), whereas the amount of quenched complexes increases substantially upon oligomerization.

Table S1. Energy transfer lifetimes, relative occurrence and trapping lifetimes for the different emissive states observed in monomeric and aggregated KO612 CP29 at RT and 77 K (see Figures S20 and S25 for further discussion). For the monomer parameters, only the amplitude and lifetime of the strongly quenched 680-nm component as obtained from TCSPC measurements is shown (see Figures S11 and Mascoli et al.[1]). For such measurements, the presented error represents 95% confidence intervals. The aggregate parameters refer to the time-resolved fluorescence data presented in Figures S12, S14, S18 and S23 and to the model described in the text, as well as the spectral components displayed in Figures S20 and S25. The mean value and uncertainty (expressed as standard deviation) were estimated from a clustered analysis of all parameter configurations yielding a fitting standard error within 2% from the best fitting. Note that, for all energy transfer acceptor-donor couples, only the transfer time for the slower (uphill) process is listed, as the transfer time downhill and isoenergetic transfers was fixed to 25 ps at RT and 32 ps at 77 K (see Methods section). An additional term in the fitting was the number of uncoupled antennae estimated from the long-lived portion of the 680-trace (last column).

	$\tau_{680,q\rightarrow680,unq}$ (ns)	$\tau_{690\rightarrow680,unq}$ (ns)	$\tau_{700\rightarrow680,unq}$ (ns)	% 680,q	% 690	% 700	$\tau_{680,q}$ (ps)	% detached
Mon. RT	/	/	/	9 ± 1	/	/	200 ± 30	
Aggr. RT [model 1]	8.1 ± 1.2	/	0.11 ± 0.01	4.9 $\pm$ 0.1	/	8.7 ± 0.3	34 ± 1	3.5 $\pm$ 0.2
Aggr. RT [model 2]	8.0 ± 0.5	/	7.6 ± 0.3	31 ± 1	/	8.9 ± 0.3	153 ± 1	$9.9 \pm$ 0.1
Mon. 77 K	/	/	/	9 ± 1	/	/	330 ± 50	
Aggr. 77 K	2.9 ± 0.3	7.6 ± 0.3	> 100	23 ± 1	16.5 $\pm$ 0.3	1.8 ± 0.0	61 ± 2	5.5 $\pm$ 0.2

Table S2. Energy transfer lifetimes, relative occurrence and trapping lifetimes for the different emissive states observed in monomeric and aggregated CP29 KO 603 at RT and 77 K (see Figures S21 and S24 for further discussion). For the monomer parameters, only the amplitude and lifetime of the strongly quenched 680-nm component as obtained from TCSPC measurements is shown (see Figures S11 and Mascoli et al.[1]). For such measurements, the presented error represents 95% confidence intervals. The aggregate parameters refer to the time-resolved fluorescence data presented in Figures S13, S15, S19 and S24 and to the model described in the text, as well as the spectral components displayed in Figures S21 and S26. The mean value and uncertainty (expressed as standard deviation) were estimated from a clustered analysis of all parameter configurations yielding a fitting standard error within 2% from the best fitting. Note that, for all energy transfer acceptor-donor couples, only the transfer time for the slower (uphill) process is listed, as the transfer time of all downhill and isoenergetic transfers was fixed to 25 ps at RT and 32 ps at 77 K (see Methods section). An additional term in the fitting was the number of uncoupled antennae estimated from the long-lived portion of the 680-trace (last column). The lifetime and amplitude in parenthesis for the quenched monomers at RT are estimates from previous transient absorption measurements[1]. Note that for this mutant the lower limit of $\tau_{680,q}$ was set to 50 ps, as otherwise the fit converged to even lower values, albeit with similar error (see also caption of Figure S21).

	$\tau_{680,q\rightarrow680,unq}$ (ns)	$\tau_{690\rightarrow680,unq}$ (ns)	$\tau_{700\rightarrow680,unq}$ (ns)	% 680,q	% 690	% 700	$\tau_{680,q}$ (ps)	% detached
Mon. RT	/	/	/	14 ± 1 (15)	/	/	90 ± 30 (60)	
Aggr. RT	2.2 ± 0.4	/	3.3 ± 0.6	36 ± 1	/	8.0 ± 0.3	50 ± 0	1.1 ± 0.1
Mon. 77 K	/	/	/	13 ± 1	/	/	200 ± 30	
Aggr. 77 K	2.9 ± 0.2	7.6 ± 0.2	> 100	31 ± 1	18.8 ± 0.4	1.6 ± 0.1	50 ± 0	2.6 ± 0.2

Text S1

Details on the modeling of kinetic traces from MCR analysis. The spectrum of the quenched complexes was assumed to be the same as that of blue unquenched complexes, based on the findings from measurements on CP29 monomers. As a result, the kinetic trace of the blue component from MCR (Figures 4b and 4e) was reconstructed as the sum of the population profiles of blue quenched and unquenched complexes in the aggregate. The lifetime of unquenched complexes was set to 4 ns (close to the longest lifetime found in unquenched monomers) to reduce the number of parameters in the model and that of quenched complexes was a fitting parameter. The moderately quenched component observed in the measurements on monomeric CP29 was neglected in our model (i.e. only the two extreme blue states with very long and very short lifetimes were considered in the aggregate description). This choice is motivated by the low occurrence of the intermediate-lifetime state in the monomers and by the fact that the lifetimes in the nanosecond range are more difficult to estimate from the fitting, which relies on much shorter-lived traces (the blue component always decays in 100–200 ps). For similar reasons, the lifetime of the red-emitting species (intermediate and far-red) was also fixed to 4 ns. Again, we cannot exclude that the actual lifetime of these states, especially at RT, exhibits shorter values and/or some heterogeneity, but based on the raw data, red-emitting states can be safely ruled out as strong quenchers, as their population remains small at RT and their lifetime is clearly longer at 77 K, when they act as deep long-living fluorescing traps. In fact, reducing the lifetime of FR to 3 ns did not result in any notable changes in the calculated kinetics.

In addition, an extra component accounting for a small fraction of long-lived energetically uncoupled antennae was included in the fitting to reproduce the residual (and always minor) long-lived contribution to the trace of the blue component from MCR (see Table 1 and S1-2). This can be explained by a relatively small number of antennae which did not aggregate and maintained, therefore, the typical long lifetime and spectrum of the blue unquenched component.

In order to reduce the number of free parameters, the hopping rates for isoenergetic or downhill energy transfer (for instance, from blue unquenched to blue quenched or to redshifted complexes, which are expected to have lower excited state free energy) were also fixed to a value of $(25\ \text{ps})^{-1}$ at RT and $(32\ \text{ps})^{-1}$ at 77 K. The same assumptions (and values) were used in the work on LHCII aggregates[2] and are in agreement with previous experimental findings[3]. For aggregates of CP29, which as a monomer has a higher number of low energy chlorophylls than LHCII[4], the hopping between adjacent units might be faster. The hopping rate might also change to some extent in the absence of Chls 612 or 603 in the corresponding KO mutants. Figure S9 shows that the effects of the possible variations of the hopping rate on the fluorescence kinetics are rather small. The effect of different arrangements of the lattice (hexagonal vs rectangular) was investigated previously[2] and was shown to be also rather small. Therefore, our approximations made to model excitation energy transfer in the aggregate are not expected to substantially affect the main results of our simulations, i.e. the relative amounts and free energy order of each fluorescent state, as well as the trap lifetime. To account for the fluctuating properties of the LHC units, the excited

state kinetics of each species were calculated and then averaged over random distributions of the various complex types within the aggregate as well as the actual numbers of these specific complexes per aggregate. The number of CP29 units in the aggregate was set to 100 in all the performed simulations. For each fitting parameter, the mean value and uncertainty (expressed as standard deviation) were estimated from a clustered analysis of all parameter configurations yielding a fitting standard error within 2% from the best fitting.

References

1. Mascoli, V., Liguori, N., Xu, P., Roy, L.M., van Stokkum, I.H.M., and Croce, R. (2019). Capturing the Quenching Mechanism of Light-Harvesting Complexes of Plants by Zooming in on the Ensemble. Chem *5*, 1–13. Available at: https://doi.org/10.1016/j.chempr.2019.08.002.

2. Chmeliov, J., Gelzinis, A., Songaila, E., Augulis, R., Duffy, C.D.P., Ruban, A. V., and Valkunas, L. (2016). The nature of self-regulation in photosynthetic light-harvesting antenna. Nat. Plants *2*, 16045.

3. Barzda, V., Gulbinas, V., Kananavicius, R., Cervinskas, V., Van Amerongen, H., Van Grondelle, R., and Valkunas, L. (2001). Singlet-singlet annihilation kinetics in aggregates and trimers of LHCII. Biophys. J. *80*, 2409–2421. Available at: http://dx.doi.org/10.1016/S0006-3495(01)76210-8.

4. Xu, P., Roy, L.M., and Croce, R. (2017). Functional organization of photosystem II antenna complexes: CP29 under the spotlight. Biochim. Biophys. Acta - Bioenerg. *1858*, 815–822. Available at: http://dx.doi.org/10.1016/j.bbabio.2017.07.003.